Role of nanoscale AlN and InN for the microwave characteristics of AlGaN/(Al,In)N/GaN-based HEMT

© T.R. Lenka¶, A.K. Panda

National Institute of Science & Technology,
Palur Hills, Berhampur-761008, Odisha, India

(Получена 11 февраля 2011 г. Принята к печати 14 февраля 2011 г.)

A new AlGaN/GaN-based high electron mobility transistor (HEMT) is proposed and its microwave characteristics are discussed by introducing a nanoscale AlN or InN layer to study the potential improvement in their high frequency performance. The 2DEG transport mechanism including various subband calculations for both (Al,In)N-based HEMTs are also discussed in the paper. Apart from direct current characteristics of the proposed HEMT, various microwave parameters such as transconductance, unit current gain ($h_{21} = 1$) cut-off frequency (f_t), high power-gain frequency ($f_{\max}$). Masons available/stable gain and masons unilateral gain are also discussed for both devices to understand its suitable deployment in microwave frequency range.

1. Introduction

Group III-nitride high electron mobility transistors (HEMTs) are the promising devices for high power and high-frequency and high temperature applications due to superior material properties of GaN and its alloys [1,2]. So GaN-based semiconductor devices are getting much attention and become highly preferred material of many research communities worldwide in the areas of microwave and millimeter wave communications [1–5]. $Al_xGa_{1-x}N$ is a wide bandgap material and is grown over GaN, so that a two dimensional electron gas (2DEG) or quantum well is created at the heterointerface, due to the conduction band discontinuity and makes the heterostructure device a suitable candidate towards RW and microwave frequency of operation [2,3]. However, the limitations on direct current (DC) and radio frequency (RF) performance of conventional $Al_xGa_{1-x}N$/GaN-based HEMTs are well analyzed [1–5]. The limitation is primarily due to polarization-induced electric fields and current collapse in these devices [3,5].

In order to further enhance the microwave characteristics of the conventional AlGaN/GaN-based HEMTs, different heterostructures are proposed by different researchers [6–10]. It is seen that a thin layer of strained $Al_xIn_{1-x}N$ in between AlGaN and GaN epitaxial layer operates the device at higher frequency as compared to conventional AlGaN/GaN-based HEMTs [3,5]. However, obtaining the structure with a thin layer of $Al_xIn_{1-x}N$ ternary is more difficult than obtaining a thin binary layer of AlN or InN over GaN with proper crystal matching [3,5]. GaN and AlN based materials are associated with very strong inherent spontaneous and piezoelectric polarization effects, which result into a high sheet charge density (n_s) of the order of $10^{14}\,\text{cm}^{-2}$ at the heterointerface [6,7]. This is expected to give better microwave characteristics. Same is the case with InN [7].

Further, the density of 2DEG and mobility in heterostructures are the key parameters related to transport properties [11]. Due to huge charge densities are associated with the carrier transport mechanism, so that the performance of the device is degraded due to presence of several scattering mechanisms such as ionized impurity scattering, dislocations scattering (due to large lattice mismatch), phonon scattering, interface roughness scattering, alloy disorder scattering etc [11–14]. Nanoscale AlN layer introduction reduces the scattering process in the 2DEG, at the heterointerface of the $Al_xGa_{1-x}N$/GaN-based HEMTs [13–15]. Same is expected from InN also.

Keeping these in mind, the authors develop the structures for AlN-based and InN-based HEMTs, computed and compare the results obtained from both the studies. It is seen that AlN-based HEMT can operate at high frequency whereas InN-based HEMTs can give more output current [3,5,7]. Such results obtained from our computations are presented in this paper. New device structure is proposed by inserting a thin nanoscale AlN and InN layer at the heterointerface of $Al_xGa_{1-x}N$/GaN structure as shown in Fig. 1. The proposed device structure, the simulation model and its physics are discussed in section 2.

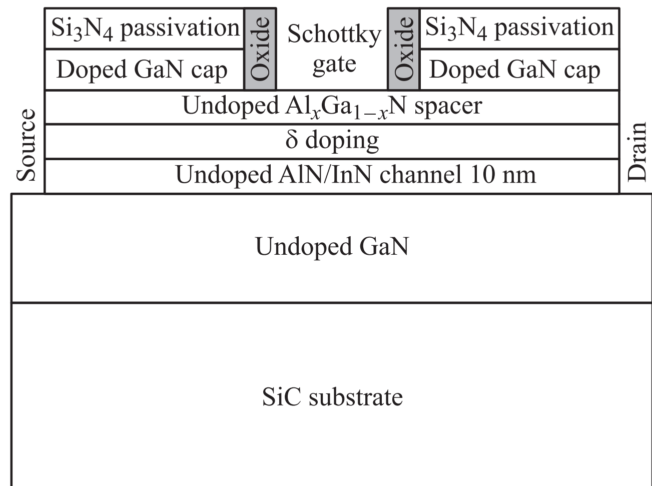

Fig. 1. Simplified structure of proposed AlGaN/AlN/GaN- and AlGaN/InN/GaN-based HEMT.

¶ E-mail: trlenka@gmail.com

Schrödinger's wave equation and Poisson's equation are also solved to determine the 2DEG concentration at the heterointerface and subband calculation [11]. This aspect is presented in section 3.

The DC, $C-V$ characteristics and microwave characteristics are discussed in section 4.

Finally a comparative performance evaluation of both devices is presented in section 5 with the conclusion.

2. Device structure and its physics

The proposed device as shown in Fig. 1 consists of several stacked layers generally grown by molecular beam epitaxy (MBE) technique [6–10]. The stacked layers include semi-insulating SiC substrate of thickness $2\,\mu$m [8], GaN layer of thickness 800 nm and over which undoped AlN or InN layer of 10 nm thickness is grown followed by another undoped barrier-layer of $Al_{0.3}Ga_{0.7}N$ of thickness 35 nm. δ-doping thickness 2 nm has been done by introducing a sheet charge of $5.4 \cdot 10^{12}\,\text{cm}^{-2}$ at a position of 31 nm of the $Al_{0.3}Ga_{0.7}N$ spacer layer. Doped GaN layer of thickness 30 nm has been deployed for the cap layer of the device. To reduce the RF-power level degradation, an insulated Si_3N_4 passivation layers of thickness 50 nm are deployed both side of the Schottky gate [6]. Better coverage of the passivation layer gives less dispersion, high gain and breakdown voltage in submicron devices and improves its perfomance [6–12].

We have considered source and drain contact length of 50 nm each and the gate length (L_g) of 250 nm. The gate is recessed to a distance of 15 nm and Schottky-gate contact having barrier potential $\phi_{Bn} = 0.9$ V has been taken in the structure. Oxide spacer of 40 nm is used as stress reliever and acts as the sidewalls of the Schottky-gate contact.

This structure is solved self consistently to show the 2DEG formation and subbands are calculated at the heterointerface where 2DEG is formed. The details of such solution and the results are presented in next section.

3. Simulation and subband calculations in the 2DEG

The growth of wide bandgap material over narrow bandgap material creates a 2DEG at the heterointerface, so that confinement of electrons in the quantum well is possible, which leads to higher mobility and resulting into a high speed device [11]. Better modulation of the 2DEG density results into high current gain cut-off frequency (f_t) and hence 2DEG is determined in this section. In order to show the formation of 2DEG and structure, we have solved the Schrödinger equation and Poisson equation self-consistently [11] incorporating both heavy hole and light holes in the simulation and are given by:

$$-\frac{\hbar}{2}\frac{d}{dx}\left[\frac{1}{m^*}\frac{d\psi_i(x)}{dx}\right] + [V(x) - E_i]\psi_i(x) = 0, \qquad (1)$$

$$\left[-\frac{\hbar^2}{2m^*}\frac{d^2}{dx^2} + V(x)\right]\psi(x) = E_i\psi(x), \qquad (2)$$

$$H\psi(x) = E_i\psi(x). \qquad (3)$$

From Eq. (2), one can obtain the equation form: $H\psi = \lambda\psi$, then the Schrödinger equation with Hamiltonian operator H is solved as follows:

$$(H - I\lambda)\psi(x) = 0, \qquad (4)$$

where λ is the eigen value, that is the eigen energy E_i in Eq. (2). Because of the determinant of $|H - I\lambda| = 0$, this indicates that $\psi_i(x)$ may have infinite dependent solutions and are shown in Fig. 2 for AlN- and InN-based HEMT.

The Poisson equation gives the idea of charge distribution in the 2DEG and is given by:

$$\nabla^2 V(x) = -\frac{q}{\epsilon}[p(x) - n(x) + N_d^+(x) - N_a^-(x)], \qquad (5)$$

$$V(x) = V_c(x) + V_{\text{H}}(x) + V_{xc}(x), \qquad (6)$$

where ϵ is the dielectric constant and N_d^+ and N_a^- are the ionized donor and acceptor densities respectively [11].

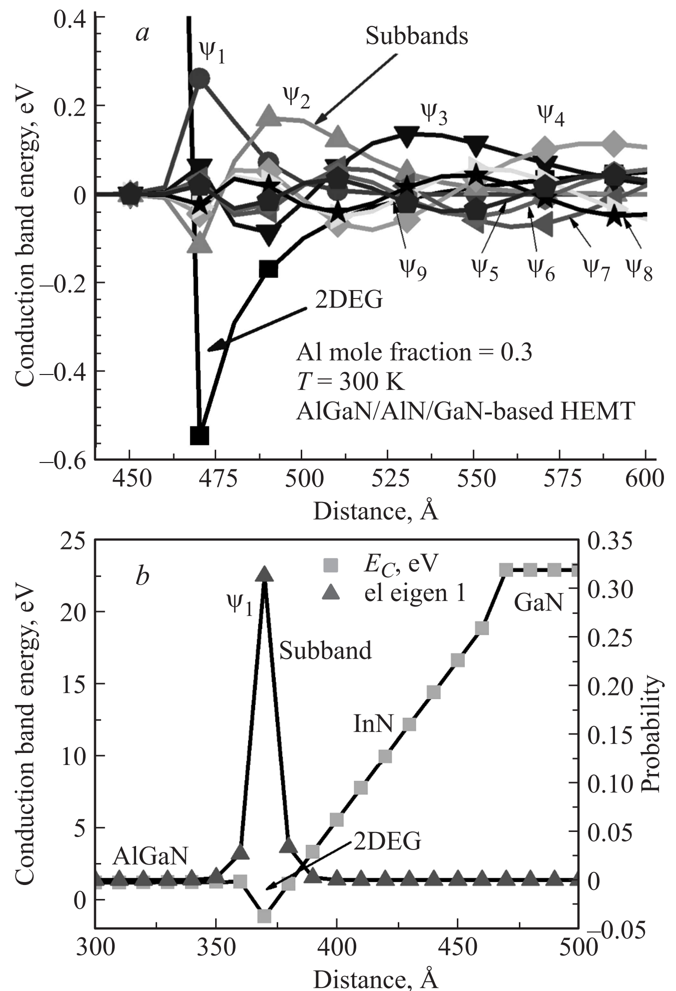

Fig. 2. Subbands in the 2DEG of AlN-based HEMT (a) and InN-based HEMT (b).

$V_c(x)$ represents the conduction-band edge potential in the form of step-function associated with the conduction-band offset at offset at the AlGaN/GaN heterojunction (depends on the Al mole fraction), $V_{\mathrm{H}}(x)$ is the Hartree potential of the electrostatic interaction due to immobile charges distrubuted in the system, and $V_{xc}(x)$ is the exchange-correlation potential representing the many-body interaction [11–15].

The one dimensional electron concentration $n(x)$ is related to the wave function and number of electrons per unit area for each energy state and is given by:

$$n(x) = \sum_i N_i |\psi_i(x)|^2, \tag{7}$$

where N_i is the number of electrons per unit area for each energy state E_i and wave function ψ_i of the i state.

N_i can be found by integrating the density of states function $g(E)$ and the Fermi–Dirac probability function $f(E)$:

$$N_i = \int_{E_i}^{\infty} g(E) f(E) dE. \tag{8}$$

For a 2DEG, the density of states (DOS) is given by $g(E) = m^*/(\pi\hbar^2)$, where m^* is the effective mass of the electron in GaN $(0.22m_0)$. Now substituting the DOS, Eq. (8) can be written as:

$$N_i = \frac{m^*}{\pi\hbar^2} \int_{E_i}^{\infty} f(E) dE,$$

$$N_i = \frac{m^*}{\pi\hbar^2} \int_{E_i}^{\infty} \frac{1}{1+\exp\left(\frac{E-E_{\mathrm{F}}}{kT}\right)} dE, \tag{9}$$

$$N_i = \frac{m^* kT}{\pi\hbar^2} \ln\left[1+\exp\left(\frac{E_{\mathrm{F}}(x)-E_i}{kT}\right)\right]. \tag{10}$$

Now putting the expression of N_i in Eq. (7), the electron concentration $n(x)$ can be derived as:

$$n(x) = \sum_i \frac{m^* kT}{\pi\hbar^2} \ln\left[1+\exp\left(\frac{E_{\mathrm{F}}(x)-E_i}{kT}\right)\right] |\psi_i(x)|^2. \tag{11}$$

A program is developed to solve the above equations self consistently and various subbands or energy states obtained for AlN and InN introduction in AlGaN/GaN-based HEMTs are determined. Some of the results are presented in Fig. 2 respectively for AlN and InN strained HEMT. It is seen from Fig. 2, *a* that more number of energy or wave functions are obtained whereas only one 2DEG state subband is formed in case of InN strained HEMT [11]. This is because the binary AlN is highly polarized rather InN material. So introduction of AlN at the heterointerface of the conventional AlGaN/GaN leads to formation of more subbands. However, the probability of finding the electrons is more in case of strained InN as shown in Fig. 2, *b*. This indicates AlN and InN strained HEMT will form better 2DEG states and hence better DC and microwave characteristics [11].

To obtain DC and microwave characteristics, we have used hydrodynamic simulation models and mobility models such as doping dependence, carrier temperature driven high field saturation [12] are incorporated in this hydrodynamic model. It solves the carrier temperature and heat flow equations in addition to the Poisson and carrier continuity equations and restricted to only one type of career. It allows the nonlocal effects as velocity overshoot and breakdown of the device to be included in the simulation. It avoids the onset of premature breakdowns due to the local field assumed in the drift-diffusion model. Various recombination models such as Auger, Shockley–Read–Hall (SRH) and radiative recombination process are also considered in the simulation model [12]. The results obtained are presented in the next section.

4. Results and discussion

The results and discussion include DC characteristics followed by capacitance voltage $(C-V)$ and microwave characteristics of the proposed device [12].

4.1. DC characteristics

The DC characteristics of the device are extracted from Technology CAD (Computer Aided Design) tool and $I-V$ characteristics are shown in Fig. 3, *a* and *b* respectively for the AlN and InN-based HEMTs. $I-V$ curves of traditional $\mathrm{Al}_x\mathrm{Ga}_{1-x}\mathrm{N}$/GaN HEMT are also drawn in Fig. 3, *a* for comparison purpose. It is seen from the figures that the drain current does not reduce, as the drain-source voltage increases. The device is simulated with the drain voltage variation from 0 to 5 V for different gate voltages varying from −0.8 to 0.8 V. The saturation drain current $(I_{d\mathrm{sat}})$ of the AlN-based HEMT device is measured to be around 600 mA/mm and 2.3 A/mm for InN-based HEMT, passivated with $\mathrm{Si_3N_4}$ passivation layer respectively. It is seen that the drain current capability of InN-based HEMT is substantially higher than the AlN-based HEMT because of less scattering occured at the heterointerface and the indium content in the alloy of $\mathrm{Al}_x\mathrm{In}_{1-x}\mathrm{N}$. Theoretical models have shown the $\mathrm{Al}_x\mathrm{In}_{1-x}\mathrm{N}$ structure to at least double the output current of $\sim \mathrm{Al_{0.2}Ga_{0.8}N/GaN}$ while maintaining a thin barrier for high frequency operation depending on the indium concentration [3,5]. The polarization induced electric field and lattice mismatch can be engineered by varying the indium content of the $\mathrm{Al}_x\mathrm{In}_{1-x}\mathrm{N}$ ternary barrier. In this device 10 nm thickness of InN and AlN channel layer is taken into consideration having bandgap of 0.8 and 6.2 eV respectively. In case of InN layer only one electron subband is present at the 2DEG, whereas in AlN layer, nine electron subbands are present as shown in Fig. 2, *a* and *b* respectively.

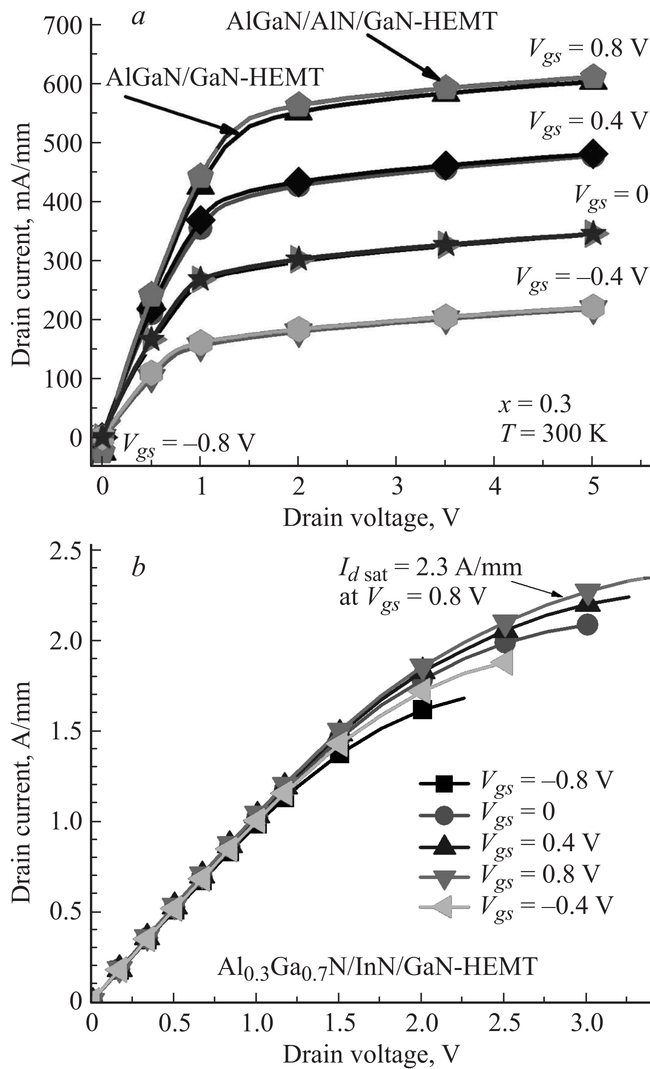

Fig. 3. Drain characteristics of AlGaN/AlN/GaN-based HEMT (*a*) and AlGaN/InN/GaN-based HEMT (*b*).

In Fig. 3, *a* it can be realized that insertion of thin AlN in the conventional AlGaN/GaN-based HEMT leads more current than the conventional $Al_xGa_{1-x}N$/GaN-based HEMT. This is in accordance with the experimental facts obtained from Mishra et al [13–15]. The improved device performance is due to its high polarization effect, reduced scattering and less 2DEG wave function penetration into the barrier.

4.2. $C-V$ characteristics

The capacitance–voltage ($C-V$) characteristics and the 2DEG shett charge density (n_s) with the variation of gate voltage from -4 to 4 V of the proposed device is shown in Fig. 4. Unlike MOSFET, the $C-V$ characteristics of HEMT also undergoes through accumulation, depletion and inversion process with the variation of gate voltage from -4 to 4 V and same type of characteristics has obtained in this case also. From Fig. 4, it is seen that, the capacitance of AlN- and InN-based HEMT decreases from $65\,\mu\text{F/cm}^2$ at a gate voltage of -4 V to a lower value and then maintained almost constant with the variation of gate voltage upto 4 V and it represents the high frequency characteristics of the device [16].

As per $C = \frac{\partial Q}{\partial V_{gs}}$, the differential change in the gate voltage in the ideal case causes a differential change in the 2DEG surface charge density at the heterointerface of AlGaN/GaN layer [16]. It is the source of electrons that produces a change in the 2DEG charge density. The electron concentration in the 2DEG cannot be changed instantaneously. If the alternating current (AC) voltage across the gate electrode changes rapidly due to its alternating nature, the change in the 2DEG density will not be able to respond so quickly. Therefore the $C-V$ characteristics is a function of frequency of the AC signal used to measure the capacitance [16]. For very high frequency of operation, the 2DEG density will not respond to the differential change in capacitor voltage, so that the capacitance is maintained constant, showing the high frequency nature [16]. Since capacitance remains constant and gate voltage increases, naturally 2DEG density increases in both the cases. There is a significant increase in the 2DEG density for InN layer at a gate voltage of around 1 V and it leads to a significant increase in the capacitance.

4.3. Microwave characteristics

The microwave characteristics are discussed with the help of two-port network analysis [17–21]. Using the same biasing and sweeping scheme as that of DC, the small-signal characteristics are analyzed for various frequencies. A mixed-mode environments is created for the AC simulation instead of simulating an isolated HEMT. That is, HEMT is embedded into an external circuit forming a two-port network. Here the voltage sources are attached to the gate (port 1) and drain (port 2) terminals. All other terminals are grounded. The small-signal output file contains the

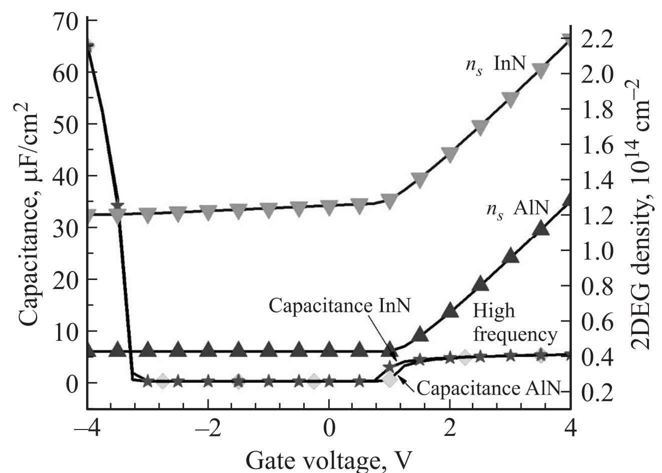

Fig. 4. Comparative $C-V$ characteristics of AlN- and InN-based HEMT.

admittance (A) and capacitance (C) matrices [19], which are equivalent to the Y-matrix as $Y = A + j\omega C$. The rows and columns of the matrices are given by the nodes in the small-signal analysis. Y-matrix obtained now can be converted to any other matrix such as S, Z or h-matrix and the microwave gain parameters such as transconductance, cut-off frequency and power gains are obtained in the following way [19–21]. The extrinsic transconductance g_m is given by:

$$g_m = \frac{\partial I_d}{\partial V_{gs}}\Big|_{V_{ds}=\text{constant}}. \qquad (12)$$

It is extracted by varying the gate voltage (V_{gq}) from -2 to 2 V with the drain–source voltage (V_{ds}) of 1 V. As seen in Fig. 5, a and b, the AlN-based HEMT passivated with Si_3N_4 material exhibits a maximum transconductance (g_m) of 275 mS/mm at a gate voltage of -0.2 V and it is 230 mS/mm at a gate voltage of -2.0 V in an InN strained HEMT. The drain currents (I_d) of AlN and InN-based HEMTs are reported to be 380 mA/mm and 1.06 A/mm respectively. In AlN-based HEMT, with the variation of gate voltage, the transconductance parameter increases with the drain current upto a peak value and then starts decreasing as the drain current reaches its maximum value in accordance with the conventional $Al_xGa_{1-x}N$/GaN-based HEMTs [13–15].

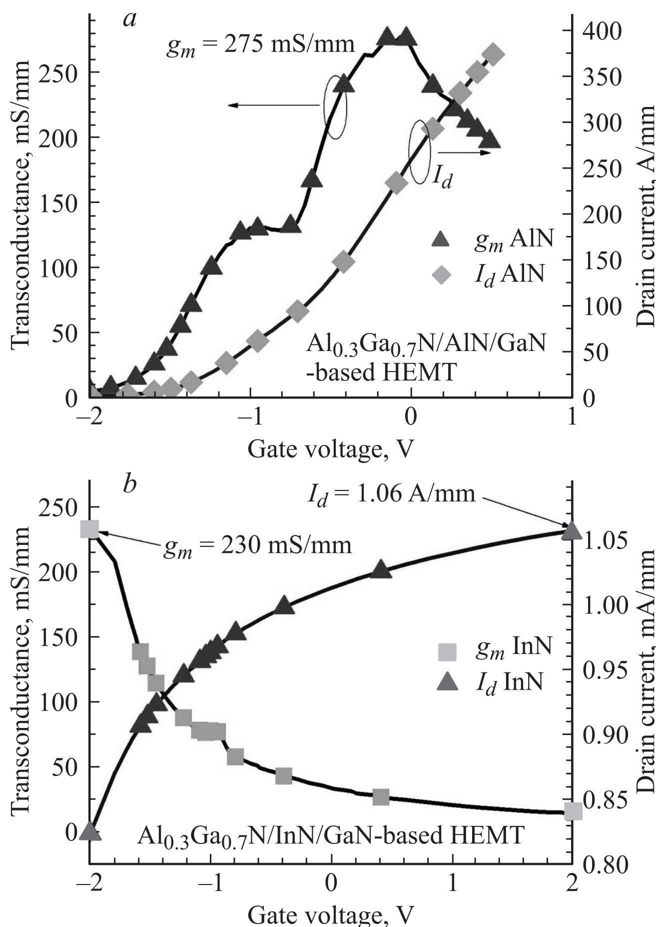

Fig. 5. Drain current (I_d) and transconductance (g_m) of AlN-based HEMT (a) and InN-based HEMT (b).

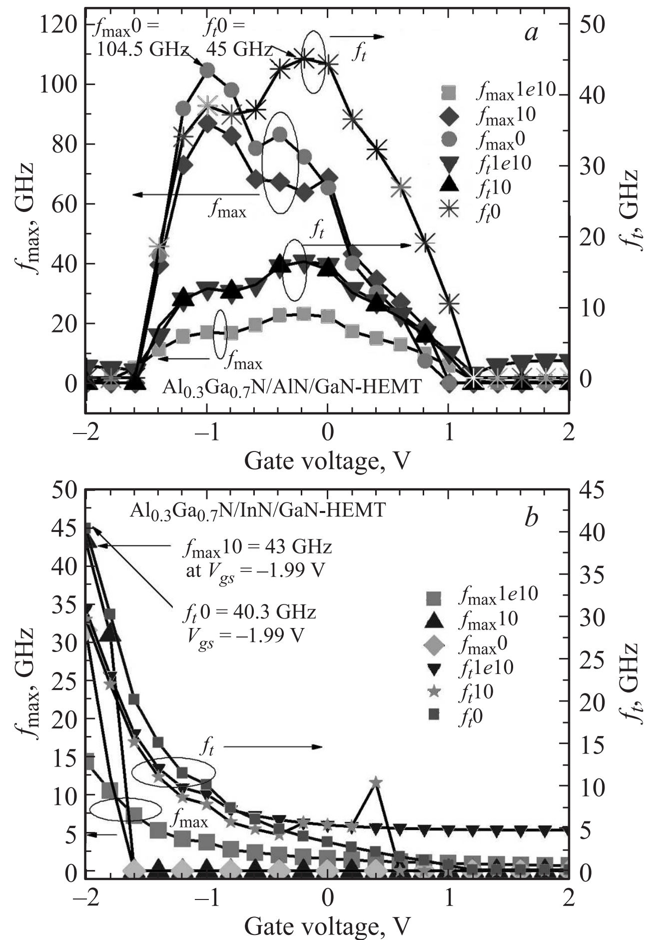

Fig. 6. Max frequency of oscillation (f_{max}) and cut-off frequency (f_t) of AlN-based HEMT (a) and InN-based HEMT (b).

But in InN-based HEMT, with the variation of gate voltage, the transconductance parameter decreases from its maximum value with the increase of drain current.

However the masons unilateral gain (MUG) can be used as a figure of merit (FOM) across all operating frequencies and its value at $f_{\max}$ is especially usefull [18–21]. $f_{\max}$ is the maximum oscillation frequency of a device and it is discovered when MUG($f_{\max}$) = 1. This frequency is also the frequency at which the maximum stable gain (MSG) and the maximum available gain (MAG) of the device become unity [18–21]. Consequently, $f_{\max}$ is a characteristic of the device, and it has the significance that it is the maximum frequency of oscillation in a circuit where only one active device is embedded in a passive network.

Similarly the cut-off frequency (f_t) as a function of transconductance (g_m) to the sum of capacitances (both gate–source capacitance, C_{gs} and gate–drain capacitance, C_{gd}) and is given as:

$$f_t = \frac{g_m}{2\pi(C_{gs} + C_{gd})}. \qquad (13)$$

Table 1. Summary of extracted frequencies

Extraction methods	AlN		InN	
	f_{max}, GHz	f_t, GHz	f_{max}, GHz	f_t, GHz
Unit-gain-point ($h_{21} = 1$)	104.5	45	32	40.3
Extract-at-dB-point	85	40	43	33
Extract-at-frequency	20	40	15	34

Three different extraction methods used to extract f_t and f_{max} from the microwave parameter matrix, such as

1) Method unit gain point (with this method, the frequency at which $h_{21} = 1$). So f_t0, $f_{max}0$ notations are used in Fig. 6.

2) Method extract-at-dB point (With this method, the frequency at which h_{21} drops by a predefined amount of decibels (dB) such as 10 dB. Then, it is assumed that the gain curve exhibits a 20 dB/decade decay at this point. The dB point at which the extrapolation is to be calculated and is set, to 10 dB here). So f_t10, $f_{max}10$ notations are used in Fig. 6.

3) Method extract-at-frequency (With this method, the extrapolation of the gain to the unit-gain-point is performed by assuming that the 20 dB/decay is established at a given frequency. Here the frequency is set to 10 GHz for extrapolation). So f_t1e10, $f_{max}1e10$ notation are used in Fig. 6.

These methods have been used to extract cut-off frequency (f_t) and maximum frequency of oscillation (f_{max}) from the microwave (S, Y, Z) parameter matrix and are shown in Fig. 6, *a*, and *b* respectively. The maximum power gain cut-off frequency, f_{max}, for AlN-based strain HEMT with Si_3N_4 passivation layer, is extracted to be 104.5 GHz, by unit-gain-point method ($f_{max}0$) at a gate voltage of -0.99 V and for InN-based strain HEMT with the same Si_3N_4 passivation layer, is 43 GHz, in a dB point method ($f_{max}10$) at a gate voltage of -1.99 V.

Similarly for AlN-based HEMT, the unit gain ($h_{21} = 1$) cut-off frequency (f_t) is measured to be 45 GHz by the unit gain method (f_t0) at a gate voltage of around -0.1 V and for the InN-based HEMT, the unit gain ($h_{21} = 1$) cut-off frequency (f_t) is measured to be 40.3 GHz at a gate voltage of -1.99 V by the same unit gain method.

The summary of frequencies in all extraction methods are enumerated in Table 1.

Unlike other signal gains, such as voltage and current gains, the power gain of the device is the ratio of an output power to an input power and is given by [17–21]:

$$\text{Power Gain} = 10\log\left(\frac{P_{out}}{P_{in}}\right) dB. \quad (14)$$

The comparative masons unilateral power gains (MUG) and current gains for AlN and InN-based HEMTs are represented in Fig. 7, *a* and *b* respectively. It is seen that for AlN-based HEMT the output power is greater than the input power, ($P_{out} > P_{in}$) from a frequency range of 100 MHz to 80 GHz and the device behaves like a power amplifier. At 80 GHz the device is behaving like an unity gain amplifier having a gain factor of unity (equivalent to 0 dB), where both input and output power are same ($P_{out} = P_{in}$). But beyond 80 GHz, it is behaving like an attenuator as the MUG is negative, so that the output is less than the input power ($P_{out} < P_{in}$). The extracted f_{max} is found to be 70 GHz from MUG curve, where MUG = 1.

Similarly for the InN-based HEMT, with the variation of frequency from 100 MHz onwards, the MUG remains negative, i. e. the output power is less that the input power ($P_{out} < P_{in}$) and the device behaves like an attenuator [19].

The current gain with the variation of frequency from 100 MHz to 100 GHz for both AlN- and InN-based HEMT is shown in Fig. 7, *b*. It is realized that for InN-based HEMT, the gain is almost constant with the variation of frequency. So this device is used as a constant current

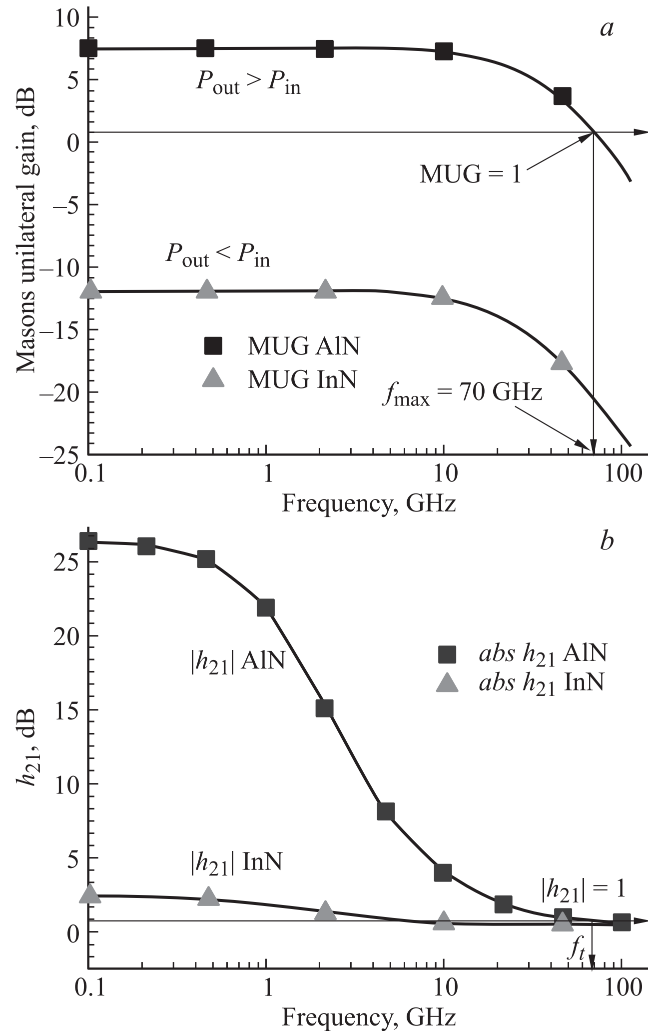

Fig. 7. MUG as a function of frequency for AlN- and InN-based HEMT (*a*) and current gain (h_{21}) as a function of frequency for AlN- and InN-based HEMT (*b*).

source at high frequency range, but in case of AlN-based HEMT, the gain is initially high and with the variation of frequency the gain decreases and then maintained almost constant. It can be used as a constant current source at low frequency range.

Similarly the maximum available power gain of a two-port network, MAG, is defined as the ratio of maximum available average power at the load to the maximum power available from the source [21]. Further the maximum available gain (MAG) and stable gains (MSG) are related as a function of Rollet stability factor (K) and is given by [18–21]:

$$\mathrm{MAG} = \mathrm{MSG}\left(K - \sqrt{K^2 - 1}\right), \tag{15}$$

where

$$\mathrm{MSG} = \left|\frac{s_{21}}{s_{12}}\right|.$$

The stability of the proposed AlN- and InN-based HEMT for a gate voltage of $V_{gs} = 0$, given in Eq. (15) are shown in Fig. 8, *a* and *b* respectively. According to the standard stability criterion of Rollet stability factor, $K > 1$, recommends the device to be unconditionally stable, for $K < 1$, the device is conditionally stable. Where as when $K = 1$, [MAG = MSG] [18–21]. In Fig. 8, *a*, for AlN-based with the variation of frequency from 100 MHz onwards, the device was initially conditionally stable and as frequency increases it is fully unconditionally stable. In the region where the amplifier is not unconditionally stable ($K < 1$), MAG is set to 18 dB and MSG is reported to be 28 dB. Where as InN-based HEMT is totally unconditionally stable over the entire frequency range as shown in Fig. 8, *b*. But in case of AlN-based HEMT, the maximum stable/available gains (MSG/MAG) are consistent upto a frequency of around 10 GHz and then it decreases with increase of frequency upto 100 GHz.

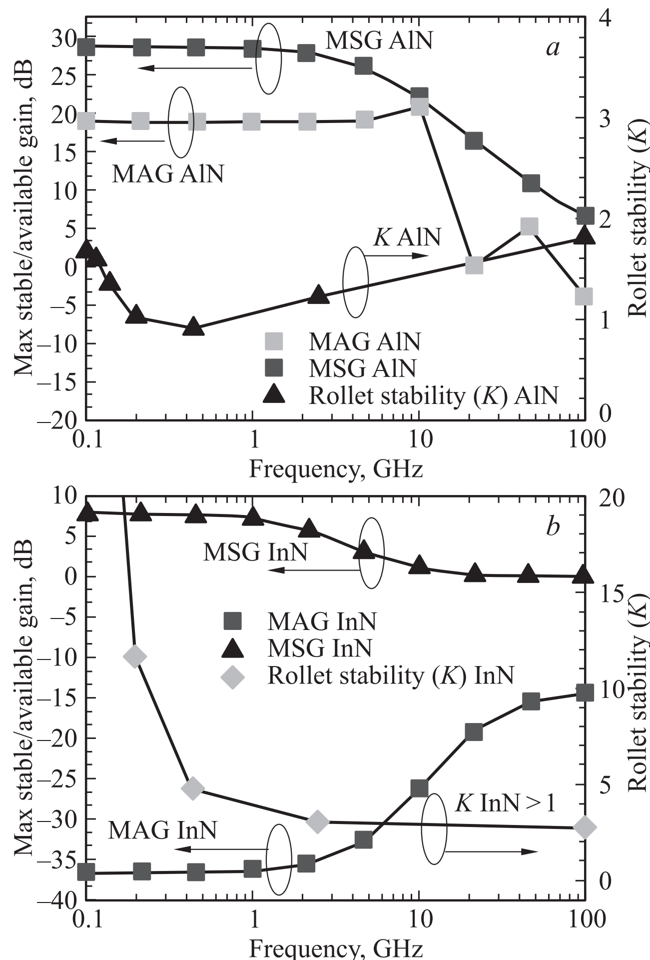

Fig. 8. MSG/MAG and rollet stability vs frequency for AlN-based HEMT (*a*) and InN-based HEMT (*b*).

But in case of InN-based HEMT, as frequency increases from 100 MHz to 3 GHz, the MSG is maintained stable to around 8 dB and MAG is maintained at −37 dB. Then MSG decreases to 0 dB and MAG increases to −15 dB with the increase of frequency. The MAG and MSG curves are quite symmetrical with the variation of frequency up to 100 GHz.

In summary it is seen that, AlN strained HEMT is better than InN strained HEMT. The symmarized comparative parameters of both strained AlN- and InN-based HEMTs are enumerated in Table 2 to understand its microwave characteristics.

Table 2. Summary of comparative parameters of AlN- and InN-based HEMTs

Parameters	AlN	InN
L_g (nm)	250	250
E_g (eV)	6.2	0.8
$f_{\max}$ (GHz)	104.5	43
f_t (GHz)	45	40.3
g_m (mS/mm)	275	230
R_{on} ($\Omega \cdot \mu$m)	0.04	0.01
n_s (cm^{-2})	$2.2 \cdot 10^{14}$	$1.3 \cdot 10^{14}$

5. Conclusion

Nanoscale AlN and InN epitaxial channel layer was introduced at the heterointerface of conventional AlGaN/GaN-based HEMT with a Si_3N_4 passivation layer over it. For a gate length of 250 nm the AlN-based HEMT demonstrates an improved transconductance of 275 mS/mm, maximum power gain cut-off frequency, $f_{\max}$, is 104.5 GHz and maximum current gain cut-off frequency, f_t, is 45 GHz rather 230 mS/mm, 43 GHz, 40 GHz of its counterpart respectively. The extracted $f_{\max}$ of AlN-based HEMT from MUG curve is reported to be 70 GHz. The AlN-based HEMT is more stable than its counterpart. It is concluded that both (Al, In)N layers in nanoscale range, are improving the 2DEG transport properties of AlGaN/GaN HEMT and makes it a suitable candidate for microwave frequency of operation. However, AlN is better than InN.

The authors acknowledge the DST-FIST & SERC fund received by National Institute of Science and Technology (NIST) from Department of Science & Technology (DST), Government of India.

References

[1] Jinwook W. Chung et al. IEEE Electron. Dev. Lett., **31** (3), (2010), doi:10.1109/LED.2009.2038935.
[2] T.R. Lenka, A.K. Panda. Int. J. Pure and Appl. Phys. (IJPAP), **6** (4), 419 (2010).
[3] K.D. Chabak et al. IEEE Electron. Dev. Lett., **31** (6), 561 (2010), doi:10.1109/LED.2010.2045099.
[4] Zhi Hong Liu et al. IEEE Trans. Electron. Dev., **57** (9), 2353 (2010), doi:10.1109/TED.2010.2054098.
[5] A. Crespo, M.M. Bellot et al. IEEE Electron. Dev. Lett., **31** (1), (2010), doi:10.1109/LED.2009.2034875.
[6] J.Y. Shiu et al. Semicond. Sci. Technol., **22** (7), 717 (2007), doi:10.1088/0268-1242/22/7/007.
[7] Md.T. Hasan et al. *5th IEEE Int. Conf. on Electron. and Comp. Engg* (ICECE-2008) p. 452.
[8] W. Luo et al. Front. Electr. Electron. Eng. China, 3 (1), 120 (2008), doi:10.1007/s11460-008-0020-8.
[9] William J. Roman. NNIN REU Research Accomplishments. (2008) p. 164.
[10] Nidhi et al. *CS-MANTECH Conf. Proc.*, May 17-20 (2010) p. 341.
[11] T.R. Lenka, A.K. Panda. Adv. Mater. Res., **159**, 342 (2010), doi:10.4028/AMR.
[12] *Synopsys User Guide Manuals* (2007).
[13] Y. Zhang, I.P. Smorchkova et al. J. Appl. Phys., **87**, 7981 (2000).
[14] I.P. Smorchkova, L. Chen et al., J. Appl. Phys., **90** (10), 5196 (2001).
[15] I.P. Smorchkova, S. Keller et al. Appl. Phys. Lett., **77** (24), 3998 (2000).
[16] X. Cheng, M. Li, Y. Wang. IEEE Trans. Electron. Dev., **56** (12), 2881 (2009).
[17] Haifeng Sun et al. Int. J. Microwave and Wireless Technol **2** (1), 33 (2010), doi:10.1017/S1759078710000164.
[18] R. Lossy et al. *Int. Conf. on Compound Semicond. Mfg., GaAsMANTECH*, Inc. (2003).
[19] T.R. Lenka, A.K. Panda. *4th IEEE Int. Conf. on Computers and Devices for Communication* (CODEC-2009) p. 1.
[20] Nikolai V. Drozdovski et al. IEEE Trans. on Microwave Theory and Techniques, **50**, (1) (2002).
[21] R.S. Carson. *High-Frequency Amplifiers* (N.Y., John Wiley & Sons, 2nd edn, 1982).

Редактор Т.А. Полянская